

A machine-learning approach for computation of fractional flow reserve from coronary computed tomography

Lucian Itu,^{1,2} Saikiran Rapaka,³ Tiziano Passerini,³ Bogdan Georgescu,³ Chris Schwemmer,⁴ Max Schoebinger,⁴ Thomas Flohr,⁴ Puneet Sharma,³ and Dorin Comaniciu³

¹Corporate Technology, Siemens SRL, Brasov, Romania; ²Department of Automation and Information Technology, Transilvania University of Brasov, Brasov, Romania; ³Medical Imaging Technologies, Siemens Healthcare, Princeton, New Jersey; and ⁴Computed Tomography-Research & Development, Siemens Healthcare GmbH, Forchheim, Germany

Submitted 3 September 2015; accepted in final form 7 April 2016

Itu L, Rapaka S, Passerini T, Georgescu B, Schwemmer C, Schoebinger M, Flohr T, Sharma P, Comaniciu D. A machine-learning approach for computation of fractional flow reserve from coronary computed tomography. *J Appl Physiol* 121: 42–52, 2016. First published April 14, 2016; doi:10.1152/jappphysiol.00752.2015.—Fractional flow reserve (FFR) is a functional index quantifying the severity of coronary artery lesions and is clinically obtained using an invasive, catheter-based measurement. Recently, physics-based models have shown great promise in being able to noninvasively estimate FFR from patient-specific anatomical information, e.g., obtained from computed tomography scans of the heart and the coronary arteries. However, these models have high computational demand, limiting their clinical adoption. In this paper, we present a machine-learning-based model for predicting FFR as an alternative to physics-based approaches. The model is trained on a large database of synthetically generated coronary anatomies, where the target values are computed using the physics-based model. The trained model predicts FFR at each point along the centerline of the coronary tree, and its performance was assessed by comparing the predictions against physics-based computations and against invasively measured FFR for 87 patients and 125 lesions in total. Correlation between machine-learning and physics-based predictions was excellent (0.9994 , $P < 0.001$), and no systematic bias was found in Bland-Altman analysis: mean difference was -0.00081 ± 0.0039 . Invasive FFR ≤ 0.80 was found in 38 lesions out of 125 and was predicted by the machine-learning algorithm with a sensitivity of 81.6%, a specificity of 83.9%, and an accuracy of 83.2%. The correlation was 0.729 ($P < 0.001$). Compared with the physics-based computation, average execution time was reduced by more than 80 times, leading to near real-time assessment of FFR. Average execution time went down from 196.3 ± 78.5 s for the CFD model to $\sim 2.4 \pm 0.44$ s for the machine-learning model on a workstation with 3.4-GHz Intel i7 8-core processor.

machine learning; synthetic database; coronary artery disease; FFR; CCTA

NEW & NOTEWORTHY

We discuss a deep-learning-based approach for noninvasive computation of coronary fractional flow reserve (FFR) from computed tomography images. The deep-learning model is trained on a large database of synthetic vessel trees, followed by verification and validation against an existing physics-based model, as well as invasive measurements. The model exhibited high diagnostic accuracy when compared against invasively measured FFR. Average execution time was 2.4 ± 0.44 s, giving real-time assessment of FFR on standard workstations.

CARDIOVASCULAR DISEASE is the leading cause of death, globally. Of these deaths, $\sim 42\%$ are caused by coronary artery disease (CAD) (59). CAD patients suffer from a buildup of plaque in the coronary arteries, which results in a corresponding decrease of blood flow to the cardiac muscle, especially under stress. In severe cases, this reduction in flow could result in myocardial ischemia and potentially death.

Previous investigations have shown that revascularization of blocked coronary arteries is preferred for severe lesions, whereas mild to moderate lesions are best treated using medical therapy alone (11). The decision to revascularize blocked coronaries is commonly performed, considering anatomical markers extracted from invasive coronary angiography, such as the percentage reduction in lumen diameter. Invasive coronary angiography is the gold standard in CAD imaging (27, 44). Subjective assessment of angiographically apparent CAD is inadequate due to high degrees of intraobserver and interobserver variability. Hence, the significance of coronary stenoses is routinely assessed by computer-assisted quantitative coronary angiography (35).

There is strong evidence that this approach has a limited accuracy in evaluating the hemodynamic significance of lesions (51). Due to the tremendous improvement in medical imaging technologies, noninvasive imaging plays an increasingly important role in the diagnosis of CAD. Coronary computed tomography angiography (CCTA) is a noninvasive imaging modality that is being increasingly used for the visualization and diagnosis of CAD, before invasive catheterization. While CCTA-based measurements of lesion anatomy correlate well with those from angiography, many severe lesions indicated by CCTA do not cause ischemia, leading to patients being unnecessarily referred to coronary angiography for invasive evaluation (17, 30). In view of the limitations of the pure anatomical evaluation of CAD, the functional index of fractional flow reserve (FFR) has been recently introduced as an alternative. FFR is defined as the ratio of flow in the stenosed branch at hyperemia, a condition of stress, with maximum coronary blood flow, to the hypothetical hyperemic flow in the same branch under healthy conditions. This can be shown to be closely approximated by the ratio of hyperemic cycle-averaged pressure distal to the stenosis to the cycle-averaged aortic pressure (41). Following multiple successful clinical trials that showed the superiority of FFR-guided decision making (50), FFR is currently the gold standard for determining the functional severity of a lesion (14, 58). Clinical evaluation of FFR is done under angiographic guidance, using a catheter-based pressure transducer. Despite the advantages offered by FFR, the use of FFR is still relatively uncom-

Address for reprint requests and other correspondence: S. Rapaka, Medical Imaging Technologies, Siemens Healthcare, 755 College Rd. E, Princeton, NJ 08540 (e-mail: saikiran.rapaka@siemens.com).

mon (39) due to additional costs, the need to administer drugs to induce hyperemia, and the invasive nature of the measurement (54).

Recently, blood flow computations performed using computational fluid dynamics (CFD) algorithms in conjunction with patient-specific anatomical models extracted from medical images, e.g., computed tomography (CT) scans of the heart and the coronary arteries, have shown great promise in being able to predict invasive, lesion-specific FFR from patient's medical images taken at resting conditions (9, 24, 32, 33, 36, 38, 43, 53). The CFD-based models combine geometrical information extracted from medical imaging with background knowledge on the physiology of the system, encoded in a complex mathematical fluid flow model consisting of partial differential equations, which can be solved only numerically. This approach leads to a large number of algebraic equations, making it computationally very demanding (48). Typically, the solution of these models requires a few hours on powerful clusters for high-fidelity models representing the complete three-dimensional velocity field to minutes on a workstation for reduced-order models, which solve for time-varying pressure and flow rate in each branch (13, 18).

The computationally demanding aspect of these CFD models and associated image segmentation process prevent adoption of this technology for real-time applications, such as intraoperative guidance of interventions. An alternative approach with high predictive power is based on machine-learning (ML) algorithms. In this case, the relationship between input data, e.g., the anatomy of a vascular tree, and quantities of interest, e.g., FFR, is represented by a model built from a database of samples with known characteristics and outcome (7). Once the model is trained, its application to unseen data provides results almost instantaneously. Such ML models have been used successfully in many medical imaging applications, including automatic heart isolation (61) and segmentation of different organs (62). This approach has also been used to reproduce the predictive capability of complex, nonlinear computational models (28, 49), resulting in a significant reduction in computational requirements compared with the original model.

In this paper, we present a ML model for FFR computation as an alternative to CFD-based modeling and show that the performance of the model is statistically not discernible from that of the CFD approach. The model is trained using a synthetically generated database of 12,000 coronary anatomies, resulting in a rich sampling of the different morphologies of coronary blockage. For each generated coronary tree, stenoses are randomly placed among the different branches and bifurcations. A reduced-order CFD model (18) is used to compute the pressure and flow distribution for each coronary tree. Subsequently, for each location along the coronary tree, we extract quantitative features describing the anatomy as well as the computed FFR value at that location. A ML model is then trained to learn the relationship between the anatomical features and the FFR value computed using the CFD model. Once the model is trained, the computational time for predicting the FFR value for a new case is significantly lower than that of the CFD model, going from 196.3 ± 78.5 s for the CFD model to around 2.4 ± 0.44 s for the ML model on a workstation with 3.4-GHz Intel i7 8-core processor.

In the rest of the paper, we refer to a computed FFR value by $cFFR$ and distinguish between $cFFR_{CFD}$, computed with a CFD method, and $cFFR_{ML}$, computed with the proposed ML method. We assess the performance of the proposed ML-based approach in three steps: 1) comparison against CFD predictions on synthetic coronary trees; 2) comparison against CFD predictions on a set of 87 patient-specific coronary anatomies; and 3) comparison against invasively measured FFR for the same 87 patients. We show that, when evaluated against invasive FFR measurement as the gold standard, $cFFR_{ML}$ is statistically not discernible from $cFFR_{CFD}$ as a diagnostic indicator.

METHODS

In this section, we introduce the ML framework developed for computing $cFFR$ from coronary anatomical models. We first describe the process of generating the synthetic coronary vessel trees, which are used for training the ML model. Next, we discuss the features used to map the relationship between the coronary anatomy and the computed value of $cFFR$.

As described in *Feature extraction and training of ML algorithm* below, the ML-based model is trained offline on a large database of synthetically generated coronary anatomies. The prediction phase is an online process, whereby the algorithm computes $cFFR_{ML}$ for a given patient's data by using the learned mapping from the training phase. Given an anatomical model (i.e., lumen segmentation), the computation of $cFFR_{ML}$ is fully automatic, without requiring user intervention. The preprocessing pipeline to generate the anatomical model is semiautomatic. The system presents the user with automatically computed centerlines and luminal contours, which can then be interactively edited by the user to create the anatomical model (16). The features required for the ML algorithm are automatically extracted from the reconstructed coronary anatomical model of the patient and then used as input to the prelearned model. $cFFR_{ML}$ is computed at all locations in the coronary arterial tree, and the resulting values are visualized by color coding the anatomical model. A schematic of the workflow is shown in Fig. 1.

Generation of synthetic training database. We created a database containing 12,000 synthetically generated coronary vessel trees to reflect the anatomical variations representative of stable patients with suspected CAD. This database, used for training the ML model, is generated algorithmically using a three-step process, as shown in Fig. 2. In the first step, the skeleton of the coronary geometry is initialized, by prescribing the number of vessels at each generation of the tree. During the second step, geometric information, such as vessel radius, degree of tapering, and branch length, is prescribed for each generation of the vessel tree. The parameters representing these geometric quantities are sampled in prespecified ranges derived from published literature (Table 1): the values have been selected to cover a broad range, ensuring that a wide array of anatomical variations and their corresponding hemodynamics are covered.

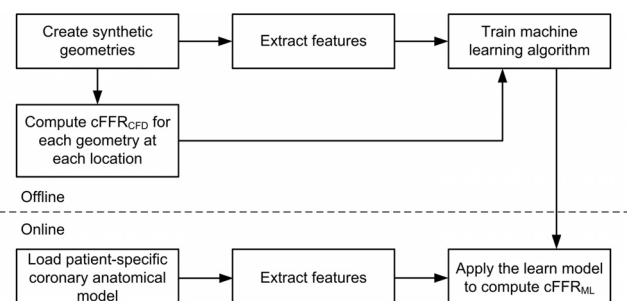


Fig. 1. Overall workflow of the proposed framework.

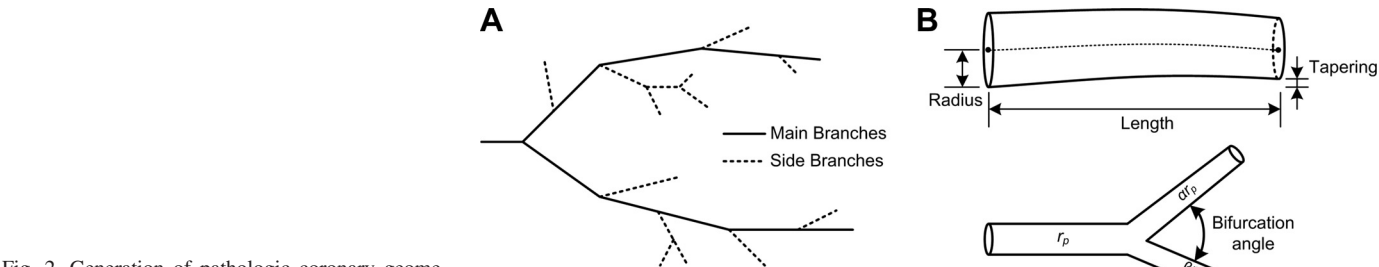


Fig. 2. Generation of pathologic coronary geometries in three steps: set up coronary skeleton (A); generate healthy geometry information (B); generate stenosis (C). r_p , Radius of the parent branch of the bifurcation.

During the third step, stenoses are generated in the coronary vessel trees. The number of stenoses on a vessel segment is sampled randomly between zero and three for a main branch segment, and between zero and two for a side branch segment. The following parameters are set for each stenosis: the maximum degree of radius reduction, the total length, the location of the stenosis center, the length of the stenosis region with minimum radius, and the overall degree of tapering along the stenosis. Stenoses are placed either on a single segment or at a bifurcation. If a bifurcation stenosis is generated, different stenosis parameter values are set for the parent and daughter branches of the bifurcation. A schematic description of the different parameters is shown in Fig. 2. The parameters describing the root radius of the left main and the right coronary artery branch and the maximum degree of radius reduction of a stenosis are sampled randomly based on a normal distribution. All other parameters are sampled with a uniform distribution.

By applying this three-step algorithm, a total of 12,000 coronary geometries were generated. The coronary geometries generated are characteristic of many common pathological situations encountered in clinical practice. However, some rare conditions like anomalous

origin of the coronary arteries and coronary artery aneurysms are not represented in this database.

CFD simulations. The target values ($cFFR_{CFD}$), required for the training phase of the ML algorithm, are computed using a reduced-order computational blood flow model, which has been previously introduced (18). The model was recently validated in clinical studies by comparing $cFFR_{CFD}$ against invasively measured FFR, and the diagnostic accuracy for the detection of functionally significant CAD was shown to be good, i.e., between 75 and 85% (3, 9, 10, 12, 26, 43, 56).

The CFD approach employs numerical methods to compute time-varying flow and pressures using the principles of fluid dynamics by solving the reduced-order Navier-Stokes equations, with blood being modeled as an incompressible fluid with constant viscosity. For the healthy nonstenotic coronary arteries, a reduced-order model is used in combination with a lumped parameter model for the coronary microvasculature (29). To enable accurate pressure computation in the stenotic regions for a given anatomical model, locally defined pressure drop models are embedded into the reduced-order blood flow model, leading to a modified hybrid reduced-order formulation. This is done to account for the complex shape of the stenosis and its impact on the pressure drop across the respective vessel segment. A systemic circulation model and a heart model are included to provide proper proximal and distal boundary conditions for the coronary circulation. For more details, we refer the reader to the APPENDIX.

The boundary conditions are estimated based on allometric scaling laws that describe the relation between form and function; the resting total coronary flow is derived from the reference radius values of the branches in the anatomical model (8, 22). The resting total coronary flow is distributed over the coronary anatomical model following Murray's law (34), and the total microvascular resistance at each outlet is determined (47) with an automatic parameter estimation algorithm (20). In the CFD model, the effect of adenosine is simulated by appropriately modifying the boundary condition, specifically by decreasing the total resistance of each coronary outlet (57). $cFFR_{CFD}$ is finally computed throughout the entire coronary artery tree as ratio of cycle-averaged pressure at the corresponding location and cycle-averaged aortic pressure.

Feature extraction and training of ML algorithm. The ML algorithm is used to compute $cFFR_{ML}$ at all locations along the centerline of the given coronary anatomical model. Hence, features are computed separately for each location along the centerline of the coronary

Table 1. Parameters with corresponding ranges used to generate synthetic coronary trees

Step	Parameter	Range
1	No. of main branches	3 (LAD, LCx, RCA)
	No. of side branches (1st generation)	2–5
	No. of side branches (2nd generation)	0–2
2	Root radius (Ref. 2)	0.15–0.35 cm
	Power coefficient (Refs. 22, 34, 60)	2.1–2.7
	Area ratio (Ref. 37)	0.35–0.45 (main branch), 0.6–0.8 (side branch)
	Degree of tapering (Ref. 63)	–20 to +5% from top to bottom
	Length (Ref. 1)	1.5–4 cm
	Bifurcation angle (Refs. 2, 21)	30–90°

LAD, left anterior descending artery; LCx, left circumflex artery; RCA, right coronary artery.

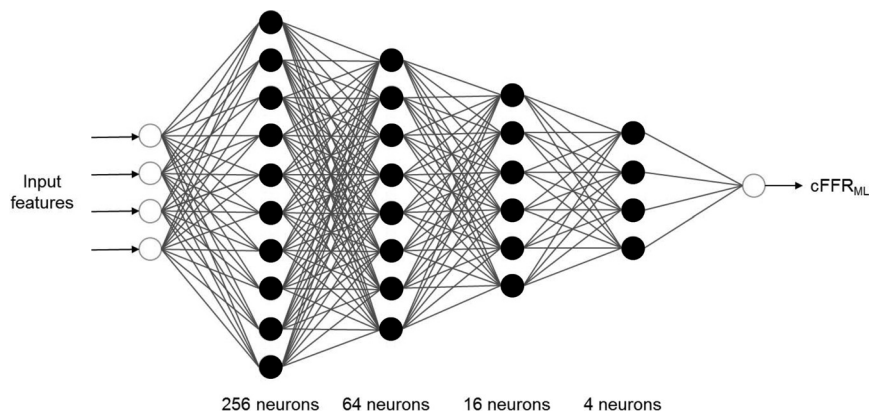


Fig. 3. Deep-learning network architecture used for training the model. The network has 4 hidden layers and uses a fully connected architecture.

geometries. Since the pressure and the flow rate at a certain location are influenced by both the upstream and the downstream circulation, the features used at each location encapsulate local, upstream, and downstream information. Upstream information is extracted along the path of the parent segments. Downstream features are computed along the path of the main branch. This path is determined automatically from the healthy reference radius of daughter branches, the number of generations downstream, and the vessel length downstream.

The ML algorithm is trained using a deep neural network with four hidden layers (shown in Fig. 3). We use a fully connected network model (5), i.e., each neuron in a layer is connected to all the neurons in the following layer, with no convolutional layers being used in this implementation. The input layer has 28 neurons corresponding to the different features computed from the coronary anatomy. The hidden layers contain 256, 64, 16, and 4 neurons, respectively, and use the sigmoidal activation function. Finally, the output layer has a single neuron with the linear activation function. To improve the model training time, each layer was initially pretrained as an autoencoder. All of the weights were initialized randomly (Xavier initialization). The entire network is optimized using a mean-squared loss function with a stochastic gradient descent algorithm. We used a highly optimized graphics processing unit implementation to speed up the training process. The original feature set based on the synthetic coronary trees was randomized and split in a 5:1 ratio, and the smaller set was used for the validation of the results. In the model training process, the algorithm was never exposed to any patient data, with training and validation being done solely with the synthetic data. The model-learning parameters, like the learning rate, momentum, etc., were adaptively refined to control the model convergence behavior.

Local geometric features. At each spatial location, the local features used are the effective radius of the vessel, the reference radius of the branch, and a segment-specific ischemic weight. The ischemic weight of each segment is a function of the set of reference radii of all the segments in the coronary tree and is defined as the potential contribution of the segment to the total ischemic burden of the patient. This initial ischemic weight is afterwards adapted, as described further down.

Upstream and downstream geometric features. To compute the features upstream and downstream, we first identify stenoses upstream and downstream. This is done with an automatic detection algorithm, including all stenoses with a degree of radius reduction larger than 10%. The stenoses are then ordered based on the degree of radius reduction. Finally, the most significant four stenoses upstream and the most significant four stenoses downstream along the main branch path are selected. For each of these, we extract the following geometric features and their nonlinear product combinations (Fig. 4):

- 1) Proximal, minimum, and distal radius.
- 2) Entrance length: length along the centerline between the start of the stenosis and the start of the segment with minimum radius.

- 3) Minimum radius length: length along the centerline between the start and the end of the segment with minimum radius.

- 4) Exit length: length along the centerline between the end of the segment with minimum radius and the end of the stenosis.

- 5) Percentage diameter reduction (DR).

$$\%DR = \left[1 - \frac{r_{\text{sten}}}{(r_{\text{prox}} + r_{\text{dist}})/2} \right] \cdot 100$$

where r_{sten} is the minimum radius of the stenosis, r_{prox} is the healthy radius proximal to the stenosis, and r_{dist} is the healthy radius distal to the stenosis.

Note that the automatic detection algorithm identifies also very mild stenoses, which individually have a small effect on the flow characteristics, but, when aggregated, may have a significant effect. At each location, we also compute aggregated values of the features described above at all upstream locations along the centerline, as well as aggregated downstream values. In addition, the upstream and downstream coronary lengths are also used as features.

In the coronary circulation, there is a significant degree of interdependence between branches. For example, in Fig. 5A, the hemodynamics at *points A and B* are influenced by the stenosis on the side branch: the presence of the stenosis leads to a decreased flow and hence to a lower pressure drop in the parent branch. This in turn influences the absolute pressure in the daughter branch to which *point B* belongs. Similarly, in Fig. 5B, the presence of the stenosis in the main branch influences the hemodynamics at *point C*: the stenosis leads to a lower flow and a lower pressure drop in the parent branch, and thus to different absolute pressure levels in the side branch.

To capture this interbranch dependence, the ML model has functionality to adapt the initial ischemic weights of the coronary segments, computed as described above, to account for the interaction between different branches. Specifically, the ischemic weights are made dependent on the stenosis specific features on upstream, downstream, and side branches.

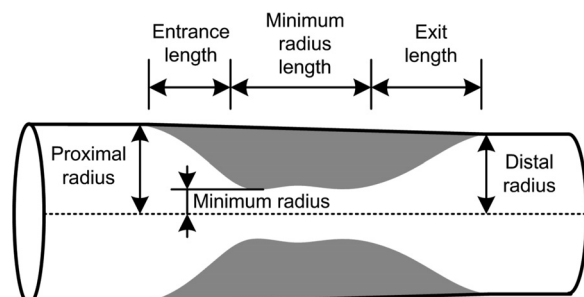


Fig. 4. Stenosis specific features.

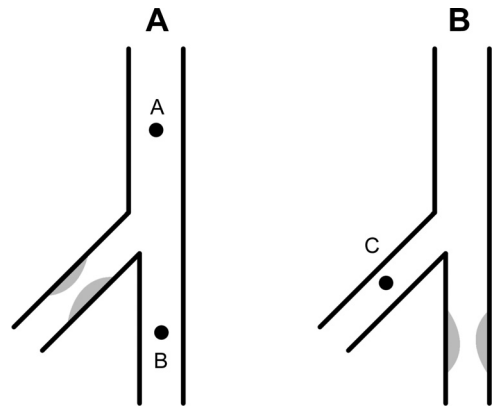


Fig. 5. Flow interaction between vessels. A: stenosis on the side branch. B: stenosis in the main branch. See METHODS for details.

RESULTS

We validated the methodology in three different steps, which are presented below.

Validation of $cFFR_{ML}$ vs. $cFFR_{CFD}$ on synthetic anatomical models. The 12,000 synthetic geometries were randomly split into six sets, whereas five of them were used for training and one for testing. We compared $cFFR_{ML}$ and $cFFR_{CFD}$ at all locations in the testing set, and the correlation was excellent in all experiments ($R = 0.9998$, $P < 0.001$). There was no systematic bias between $cFFR_{ML}$ and $cFFR_{CFD}$ (mean difference was 0.0008). When $cFFR_{CFD}$ was considered as ground truth, with a cutoff of 0.8, $cFFR_{ML}$ predicted $cFFR_{CFD}$ with an accuracy of 99.7%.

Validation of $cFFR_{ML}$ vs. $cFFR_{CFD}$ on patient-specific anatomical models. We used a database of 87 patient-specific anatomical models generated from CT data using image segmentation, following a protocol described in Refs. 9 and 43. Invasive FFR was measured for 125 lesions in these 87 patients. The FFR measurement locations were either determined from the angiogram images showing the pressure wire, or marked at a location that was approximately located 20 mm downstream from the stenosis (41). Correlation between $cFFR_{ML}$ and $cFFR_{CFD}$ was excellent (0.9994 , $P < 0.001$), and no

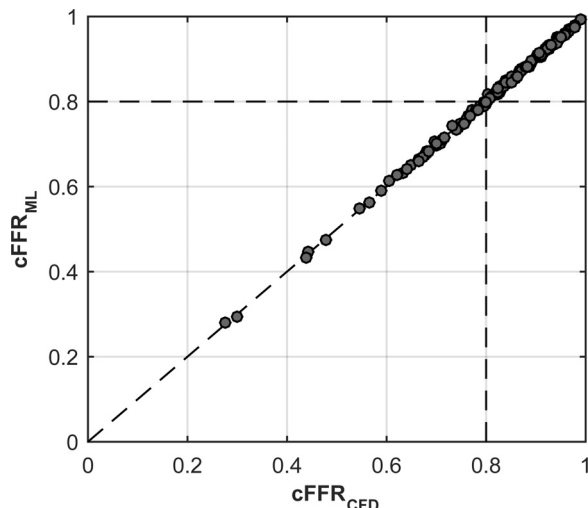


Fig. 6. Scatterplot of $cFFR_{ML}$ and $cFFR_{CFD}$ (correlation = 0.9994).

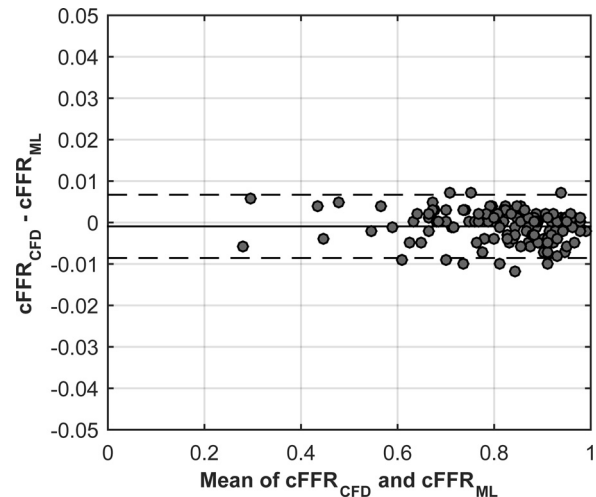


Fig. 7. Bland-Altman analysis plot comparing $cFFR_{ML}$ and $cFFR_{CFD}$ shows no systematic bias (95% limits of agreement, -0.0085 - 0.0067).

systematic bias was found in Bland-Altman analysis between $cFFR_{ML}$ and $cFFR_{CFD}$: mean difference was -0.00081 ± 0.0039 , as shown in Figs. 6 and 7. The average computation time required for computing $cFFR_{ML}$ in the entire coronary tree of one patient was 2.4 ± 0.44 s, whereas the $cFFR_{CFD}$ computations required 196.3 ± 78.5 s, both on a 3.4-GHz Intel i7 8-core CPU.

Table 2 displays a more detailed analysis of the differences between $cFFR_{ML}$ and $cFFR_{CFD}$, where the lesions have been grouped in five different bins based on the $cFFR_{CFD}$ values (0.0 to 0.6, 0.6 to 0.7, 0.7 to 0.8, 0.8 to 0.9, and 0.9 to 1.0), either for all lesions, or separately for the three main branches: left anterior descending artery, left circumflex artery, and right coronary artery. Although the mean difference slightly decreases with increasing $cFFR_{CFD}$ values, overall the variation is very small and the agreement between $cFFR_{ML}$ and $cFFR_{CFD}$ is high for all bins and all locations.

Table 2. Detailed analysis of the differences between $cFFR_{ML}$ and $cFFR_{CFD}$

Lesions	$cFFR_{CFD}$ Bin	No. Lesions	Mean Difference \pm SD
All	0.0–0.6	8	0.001 ± 0.004
	0.6–0.7	14	-0.001 ± 0.004
	0.7–0.8	23	0.000 ± 0.0040
	0.8–0.9	40	-0.001 ± 0.004
	0.9–1.0	40	-0.002 ± 0.003
LAD	0.0–0.6	6	0.000 ± 0.005
	0.6–0.7	10	-0.003 ± 0.004
	0.7–0.8	16	0.000 ± 0.004
	0.8–0.9	27	-0.002 ± 0.004
	0.9–1.0	20	-0.002 ± 0.003
LCx	0.0–0.6	2	0.002 ± 0.003
	0.6–0.7	1	0.002 ± 0.000
	0.7–0.8	4	0.001 ± 0.003
	0.8–0.9	5	-0.000 ± 0.003
	0.9–1.0	11	-0.003 ± 0.003
RCA	0.0–0.6	0	
	0.6–0.7	3	0.003 ± 0.001
	0.7–0.8	3	0.000 ± 0.004
	0.8–0.9	8	0.001 ± 0.002
	0.9–1.0	9	0.001 ± 0.002

Table 3. Diagnostic parameters in all vessels (N = 125)

	cFFR _{CFD}	cFFR _{ML}
True positive, no.	31	31
False positive, no.	14	14
True negative, no.	73	73
False negative, no.	7	7
Sensitivity, %	81.6 (66.6–90.8)	81.6 (66.6–90.8)
Specificity, %	83.9 (74.8–90.1)	83.9 (74.8–90.1)
PPV, %	68.9 (54.3–80.2)	68.9 (54.3–80.2)
NPV, %	91.2 (83.2–95.7)	91.2 (83.2–95.7)
Accuracy, %	83.2 (75.6–88.7)	83.2 (75.6–88.7)
Correlation	0.725	0.729
Mean ± SD	0.814 ± 0.135	0.815 ± 0.135

Values in parentheses are ranges. A positive event, representing a hemodynamically significant stenosis, is defined by invasive FFR ≤ 0.80 . cFFR_{CFD} diagnostic parameters are obtained with the CFD algorithm; cFFR_{ML} diagnostic parameters are obtained with the ML algorithm. PPV and NPV, positive and negative predictive values, respectively.

Diagnostic performance of cFFR_{ML} and cFFR_{CFD} vs. invasive FFR. We used the same set of 87 patients to compare the performance of cFFR_{ML} against invasively measured FFR. Invasive FFR ≤ 0.80 was regarded as criterion for positive ischemia and was found in 38 lesions out of 125. For cFFR_{ML}, sensitivity was 81.6%, specificity 83.9%, and accuracy 83.2%. Table 3 displays the diagnostic performance of cFFR_{CFD} and cFFR_{ML} vs. invasively measured FFR, with corresponding 95% confidence intervals. The overall correlation between cFFR_{ML} (0.814 ± 0.135) and invasive FFR (0.838 ± 0.11) was 0.729 ($P < 0.001$). Figure 8 displays the scatterplots of cFFR_{CFD} and cFFR_{ML} vs. invasive FFR, while Fig. 9 displays the Bland-Altman analysis between cFFR_{CFD}/cFFR_{ML} and invasive FFR. The close overlap between the two methods further demonstrates the statistical equivalence of the two approaches.

In Figs. 10–12, representative case examples are shown, illustrating the almost perfect agreement between the two algorithms at each point on the coronary tree. The receiver-operator characteristic curves for cFFR_{CFD} and cFFR_{ML} are presented in Fig. 13. The area under the curve was 0.90 for both cFFR_{CFD} and cFFR_{ML}.

DISCUSSION

We have introduced a ML algorithm for a workstation-based near real-time computation of FFR from anatomical models

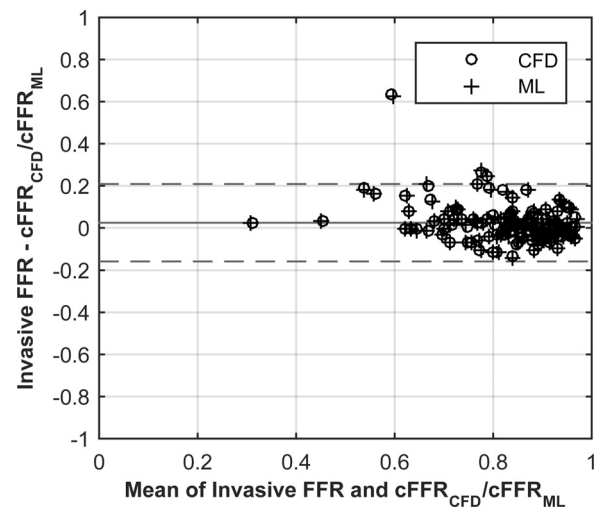


Fig. 9. Bland-Altman analysis plot comparing cFFR_{CFD} and cFFR_{ML} vs. invasive FFR (cFFR_{CFD} 95% limits of agreement, -0.159 – 0.207 ; cFFR_{ML} 95% limits of agreement, -0.159 – 0.206).

extracted from CCTA. Similar to previously published approaches based on computational modeling, our approach provides a noninvasive assessment of FFR from routinely performed CCTA scans. To the best of our knowledge, our methodology represents the only currently available solution for noninvasive, near real-time computation of FFR in the entire coronary tree. Other approaches reported in literature required several minutes (43) to several hours (36) for execution of the FFR algorithm. Our approach is potentially well-suited for a clinical setting, since it is computationally efficient in terms of both execution speed and hardware requirements and is based on anatomical data acquired from routine CCTA. The diagnostic accuracy of our algorithm (83%) is in the same range as that of previously published data on FFR computed from CCTA images, which varied from 73 to 85% (9, 12, 26, 24, 32, 36, 43). As more data are emerging from such studies, the incremental diagnostic value of cFFR over the traditional CCTA-based visual or quantitative lesion grading is becoming more evident. As a result, this technology has the potential to further strengthen the role of CCTA as a gatekeeper to the catheterization laboratory.

Previous studies have tried to assess the functional significance of CAD from geometric features of the stenosis, with

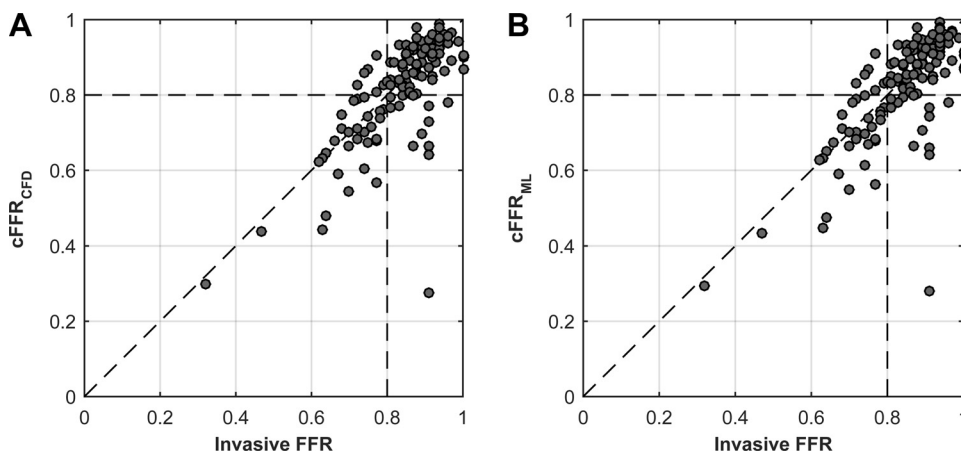
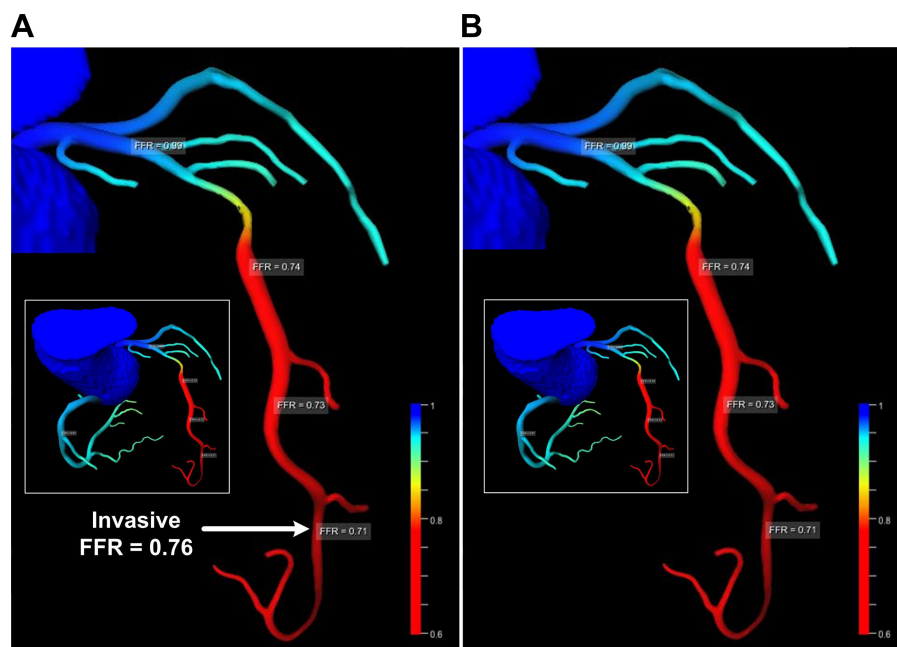


Fig. 8. A: scatterplot of cFFR_{CFD} and invasive FFR (correlation = 0.725). B: scatterplot of cFFR_{ML} and invasive FFR (correlation = 0.729).

Fig. 10. Case example of a coronary anatomical model reconstructed from CT data. *A*: $cFFR_{CFD}$ map of the entire coronary tree, including a close-up view of the left anterior descending artery (LAD), with invasive FFR = 0.76 and $cFFR_{CFD}$ = 0.71. *B*: $cFFR_{ML}$ map of the entire coronary tree, including a close-up view of the LAD, with $cFFR_{ML}$ equal to $cFFR_{CFD}$ at the invasive FFR measurement location.



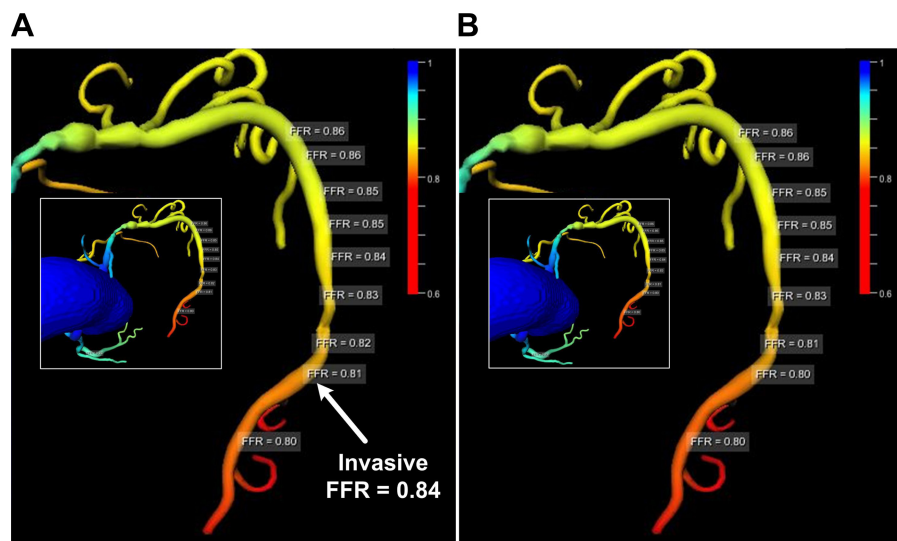
limited success (4, 15, 25). Herein, however, we use a comprehensive set of geometric features describing not only the stenotic region, but the entire coronary arterial tree. Combined with state-of-the-art ML techniques, our approach demonstrates that geometric features alone can be used as predictors of patient-specific hemodynamic states, without the need of explicitly solving the hemodynamics equations.

The key ingredients for the design of our ML method are the availability of a comprehensive database of training data, as well as the proper selection of features that are most significant for the predicted quantity. In an ideal scenario, the training database would consist of thousands of anatomical models extracted from CCTA images, accounting for the variability of coronary vessels across different patient populations and the corresponding invasive FFR measurement of each lesion. From a practical point of view, establishing such a large database would be prohibitively expensive and time-consuming.

To address this issue, we introduced the concept of a training database consisting of synthetically generated vascular geometries representing the coronary tree, and corresponding FFR values computed from a CFD algorithm at all locations of the coronary tree. The synthetic database is parameterized on the morphological features of the vascular tree, allowing the proper sampling of relatively uncommon configurations, such as serial stenoses, multibranch stenoses, bifurcation stenoses, diffuse disease, or rare pathological conditions. After training, the ML algorithm encodes the correlation between the set of chosen geometric features and the quantity of interest, herein FFR, predicted by the validated CFD model. In the population on which the algorithm was tested, the patient anatomical features were well within the region of high confidence for the ML algorithm.

Our approach can also be extended to compute other hemodynamic quantities, such as coronary flow reserve, rest distal

Fig. 11. Case example of a coronary anatomical model reconstructed from CT data. *A*: $cFFR_{CFD}$ map of the entire coronary tree, including a close-up view of the right coronary artery (RCA), with invasive FFR = 0.84 and $cFFR_{CFD}$ = 0.81. *B*: $cFFR_{ML}$ map of the entire coronary tree, including a close-up view of the RCA, with $cFFR_{ML}$ = 0.80 at invasive FFR measurement location.



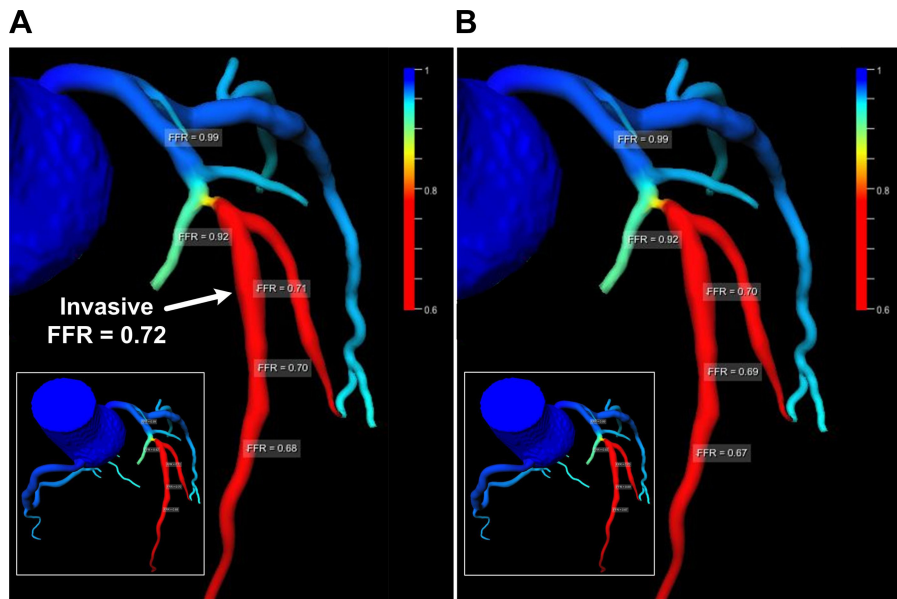


Fig. 12. Case example of a coronary anatomical model reconstructed from CT data. A: $cFFR_{CFD}$ map of the entire coronary tree, including a close-up view of the LAD, with invasive FFR = 0.72 and $cFFR_{CFD}$ = 0.71. B: $cFFR_{ML}$ map of the entire coronary tree, including a close-up view of the LAD, with $cFFR_{ML}$ = 0.70 at invasive FFR measurement location.

coronary pressure-to-aortic pressure ratio (23), the instantaneous wave-free ratio (46), hyperemic/basal stenosis resistance (31, 55), or shear stress (45), each of which can be used as a ground-truth in the training database.

Additionally, the set of features can be expanded to include other characteristics of the vascular tree, e.g., plaque composition, or even information such as the clinical history of the patient, that could play a role in determining the functional significance of a lesion and its stability over time (40).

It should be noted that the presented approach is generic with respect to the CFD model used for training the algorithm. For this work, we used a reduced-order CFD approach to generate the training database.

On the other hand, our results also point to the fact that the accuracy of $cFFR_{ML}$ will depend on the accuracy of the CFD model used in the training phase. In general terms, the performance of our method is expected to be statistically equivalent to that of the CFD model.

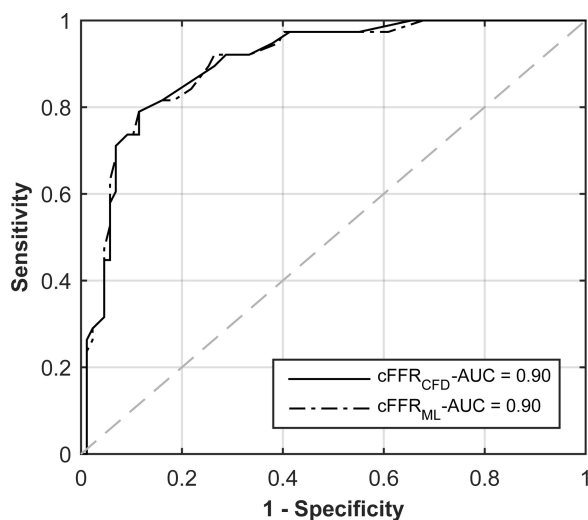


Fig. 13. Receiver-operator characteristic curves for 189 vessels, as obtained with $cFFR_{CFD}$ and $cFFR_{ML}$. AUC, area under the curve.

Since the ML algorithm computes $cFFR$ at all locations of a coronary tree, a natural extension of this work is to generate virtual pull-back curves, where the variation of $cFFR$ along a path from ostium to a distal coronary location is depicted. Such an analysis could be useful for determining the most significant lesion in case of serial stenoses.

Our study has a number of limitations. Since the proposed ML algorithm learns the output of a computational blood flow model, with almost perfect results, the limitations are mainly given by the limitations of the blood flow model. First of all, although the set of patient geometries used herein comprises a significant amount of lesions, further clinical studies are required for extensive validation of the methodology. In the present study, the majority of lesions had an invasive FFR between 0.7 and 1.0 (only 11 lesions had an FFR < 0.7) and further validation of the model is required under different conditions. However, the most difficult lesions in terms of classification are those that are close to the cutoff value of 0.8. In this regard, one interesting study base was recently conducted (26): $cFFR_{CFD}$ thresholds of 0.74 and 0.87 were determined for which positive and negative predictive values, respectively, were both >90%. Hence, in the proposed hybrid approach, $cFFR_{CFD}$ > 0.87 was used to defer revascularization, $cFFR_{CFD}$ < 0.74 to confirm treatment, while lesions with intermediate $cFFR_{CFD}$ values were classified based on invasive FFR. The hybrid approach resulted in an overall 95% agreement with the FFR-only strategy and would potentially obviate the need for invasive pressure measurements in 50% of the patients.

Second, the definition of the parameters of the blood flow model uses physiological assumptions, which would also require validation on larger data sets. Such assumptions include, for example, the allometric scaling laws applied for estimating the flow rate distribution, the effect of hyperemia (for patients with microvascular disease, the decreased effect of a hyperemia-inducing drug may lead to an underestimation of the FFR value), the use of population-averaged rheological properties of the blood, etc. Moreover, the collateral circulation has not been taken into account. Collaterals can have a significant

impact on the hemodynamics, especially for very severe lesions.

Properties of blood, such as density and viscosity, also influence the pressure losses. This dependence has not affected the comparison between CFD and ML results in this paper, since the same constant density and viscosity were used for the CFD computations in synthetic and patient-specific geometries. Such parameters can also be easily incorporated into the ML model by appropriately sampling over these variables in the synthetic database.

The models used for generating the synthetic coronary trees are representative of many commonly occurring clinical cases. However, the database, as used in this paper, does not contain less frequent pathological conditions, like anomalous origin of the coronary arteries and coronary artery aneurysms. Furthermore, the shapes of the stenosis used to generate the synthetic vessel trees are of a smooth nature and do not account for the noise typically found in medical images. This issue can be addressed by augmenting the database with noisy variants of the geometries to improve model robustness.

Finally, an important limitation in leveraging the real-time capabilities of the algorithm is the time required for data preparation, i.e., the generation of the coronary anatomical model, which varies between 10 and 60 min. In this study, we did not systematically evaluate the time spent in model preparation (i.e., lumen segmentation), but in a different preclinical study using the same preprocessing pipeline as the one used in this paper (43), a total processing time of 37.5 ± 13.8 min was reported.

In conclusion, we propose a real-time FFR computation model with high predictive power and diagnostic accuracy in detecting positive ischemia, by learning correlations that are hidden in the “big data” that are now available for each patient. As a practical application, we demonstrate how we can learn the behavior of complex physiological models with proven capability of predicting invasive FFR, using purely anatomical information available in the clinical routine.

APPENDIX: REDUCED-ORDER CFD MODEL

The reduced-order CFD model described herein has been previously introduced in Ref. 18. The model was recently validated in several clinical studies by comparing $cFFR_{CFD}$ against invasively measured FFR, and the diagnostic accuracy for the detection of functionally significant CAD was shown to be good, i.e., between 75 and 85% (3, 9, 10, 12, 26, 43, 56). Furthermore, in a recent meta-analysis of published clinical studies for CT-based FFR, the performance of the CFD model used in this paper was shown to be comparable with that of the other published CFD-based approaches (13). We also note that the reduced-order CFD model described herein has also been applied successfully in other contexts, including computation of FFR based on anatomical models reconstructed from X-ray angiography (52) and validated against clinical measurements in patients with aortic coarctation (19, 42).

The reduced-order CFD model is derived from the Navier-Stokes equations using appropriate assumptions on the nature of the flow in blood vessels. In healthy, nonstenotic coronary arteries, the flow is assumed to have a dominant component in the axial direction and axial symmetry. For axisymmetric flow, the continuity equation is:

$$\frac{\partial u_x}{\partial x} + \frac{1}{r} \frac{\partial (ru_r)}{\partial r} = 0 \quad (A1)$$

where x is the coordinate in the longitudinal direction, u is the

velocity, and r is the radius. By integrating over the cross-sectional area, while accounting for the changing vessel cross-sectional area, the following formulation is obtained:

$$\frac{\partial A(x, t)}{\partial t} + \frac{\partial q(x, t)}{\partial x} = 0 \quad (A2)$$

where t is time, $A(x, t)$ is the cross-sectional area, and $q(x, t)$ is the flow rate. For the momentum equations, we also assume that the pressure is constant within each cross section, varying primarily along the longitudinal direction. The axial momentum equation is:

$$\frac{\partial u_x}{\partial t} + u \frac{\partial u_x}{\partial x} + u_r \frac{\partial u_x}{\partial r} + \frac{1}{\rho} \frac{\partial p}{\partial x} = \frac{v}{r} \frac{\partial}{\partial r} \left(r \frac{\partial u_x}{\partial r} \right) \quad (A3)$$

where p is the pressure, ρ is the density, and v is the kinematic viscosity. By integrating over the cross-sectional area, the following formulation is obtained:

$$\frac{\partial q(x, t)}{\partial t} + \frac{\partial}{\partial x} \left(\alpha \frac{q^2(x, t)}{A(x, t)} \right) + \frac{A(x, t)}{\rho} \frac{\partial p(x, t)}{\partial x} = K_R \frac{q(x, t)}{A(x, t)} \quad (A4)$$

where the coefficients α and K_R account for the momentum-flux correction and viscous losses due to friction, respectively. To close the system of equations, we need a state equation that relates the pressure inside the vessel to the cross-sectional area. We have modeled the vessel wall as a purely elastic material, which responds to changing pressures through radial displacements:

$$p(x, t) \Psi_{el}(A) + p_0 = \frac{4Eh}{3r_0}(x) \left[1 - \sqrt{\frac{A_0(x)}{A(x, t)}} \right] + p_0 \quad (A5)$$

where E is the Young modulus, h is the wall thickness, r_0 is the initial radius corresponding to the initial pressure p_0 , and A_0 is the initial cross-sectional area. The elastic wall properties, Ψ_{el} , are estimated using a best fit to experimental data (37). The system of equations is discretized with a finite difference method and solved with the Lax-Wendroff numerical scheme.

In the stenotic regions, the simplifying assumption that the axial velocity is dominant over the radial velocity is no longer valid. Thus, to enable accurate pressure computation, a pressure-drop model is embedded into the momentum conservation equation (6). The pressure drop across the stenosis (ΔP_s) is formulated as a sum of three terms (viscous term, turbulent or Bernoulli term, and inertance term):

$$\Delta P_s = \frac{\mu K_v}{2\pi r_0^3} q + \frac{\rho K_t}{2A_0^2} \left(\frac{A_0}{A_s} - 1 \right)^2 |q| q + \frac{\rho K_u L_s}{A_0} \frac{\partial q}{\partial t} \quad (A6)$$

where μ is the dynamic blood viscosity; L_s is the stenosis length; and K_v , K_t , and K_u are the viscous, turbulent, and inertance coefficients, respectively (quantities indexed with “0” refer to the normal vessel, while “s” refers to the stenosis). The segments treated as stenosis segments are coupled to the regular segments by considering continuity of total pressure and of flow rate.

A lumped heart model (time-varying elastance model) is coupled at the inlet of the aorta to provide the inlet boundary condition. The outlet boundary conditions are provided by coronary microvascular models which account for the influence of the myocardial contraction on the flow waveform (29).

The model and methods used for personalizing it to patient conditions are described in greater detail in (18). Interested readers are referred to this publication for more details.

DISCLOSURES

L. Itu is an employee of Siemens SRL, Corporate Technology, Brasov, Romania. S. Rapaka, T. Passerini, B. Georgescu, P. Sharma, and D. Comaniciu are employees of Siemens Healthcare, Princeton, NJ. C. Schwemmer, M. Schoebinger, and T. Flohr are employees of Siemens Healthcare GmbH, Forchheim, Germany.

DISCLAIMER

The concepts and information presented in this paper are based on research and are not commercially available.

AUTHOR CONTRIBUTIONS

L.I., S.R., T.P., B.G., C.S., M.S., P.S., and D.C. conception and design of research; L.I., S.R., B.G., and P.S. performed experiments; L.I. and S.R. analyzed data; L.I., T.P., and P.S. interpreted results of experiments; L.I. prepared figures; L.I., S.R., T.P., and P.S. drafted manuscript; L.I., S.R., T.P., C.S., M.S., T.F., P.S., and D.C. edited and revised manuscript; C.S., M.S., T.F., and D.C. approved final version of manuscript.

REFERENCES

- Aharinejad S, Schreiner W, Neumann F. Morphometry of human coronary arterial trees. *Anat Rec* 251: 50–59, 1998.
- Atta-Alla S, El Sawa E, Atta-Alla A, El Baassiri E, Hassan KH. Morphometric study of the right coronary artery. *Int J Anat Res* 3: 1362–1370, 2015.
- Baumann S, Wang R, Schoepf J, Steinberg D, Spearman J, Bayer R, Hamm C, Renker M. Coronary CT angiography-derived fractional flow reserve correlated with invasive fractional flow reserve measurements—initial experience with a novel physician-driven algorithm. *Eur Radiol* 25: 1201–1207, 2015.
- Ben-Dor I, Torguson R, Gaglia MA Jr, Gonzalez MA, Maluenda G, Bui AB, Xue Z, Satler LF, Suddath WO, Lindsay J, Pichard AD, Waksman R. Correlation between fractional flow reserve and intravascular ultrasound lumen area in intermediate coronary artery stenosis. *EuroIntervention* 7: 225–233, 2011.
- Bengio Y. Learning deep architectures for AI. *Found Trends Mach Learn* 2: 1–127, 2009.
- Bessemis D. *On the Propagation of Pressure and Flow Waves through the Patient-Specific Arterial System* (PhD Thesis). Eindhoven, the Netherlands: Universiteitsdrukkerij TU Eindhoven, 2007.
- Bishop CM. *Pattern Recognition and Machine Learning*. New York: Springer, 2006.
- Choy JS, Kassab GS. Scaling of myocardial mass to flow and morphometry of coronary arteries. *J Appl Physiol* 104: 1281–1286, 2008.
- Coenen A, Lubbers MM, Kurata A, Kono A, Dedic A, Chelu RG, Dijkshoorn ML, Gijzen FJ, Ouhlous M, van Geuns RJM, Nieman K. Fractional flow reserve computed from noninvasive CT angiography data: diagnostic performance of an on-site clinician-operated computational fluid dynamics algorithm. *Radiology* 274: 674–683, 2015.
- Coenen A, Lubbers MM, Kurata A, Kono A, Dedic A, Chelu RG, Dijkshoorn ML, van Geuns RJ, Schoebinger M, Itu L, Sharma P, Nieman K. Coronary CT angiography derived fractional flow reserve: Methodology and evaluation of a point of care algorithm. *J Cardiovasc Comput Tomogr* 10: 105–113, 2016.
- De Bruyne B, Pijls NH, Kalesan B, Barbato E, Tonino PA, Piroth Z, Jagic N, Möbius-Winkler S, Rioufol G, Witt N, Kala P, McCarthy P, Engström T, Oldroyd KG, Mavromatis K, Manoharan G, Verlee P, Frobert O, Curzen N, Johnson JB, Jüni P, Fearon WF. Fractional flow reserve-guided PCI vs. medical therapy in stable coronary disease. *N Engl J Med* 367: 991–1001, 2012.
- De Geer J, Sandstedt M, Björkholm A, Alfredsson J, Janzon M, Engvall J, Persson A. Software-based on-site estimation of fractional flow reserve using standard coronary CT angiography data. *Acta Radiol*. In press.
- Deng SB, Jing XD, Wang J, Huang C, Xia S, Du JL, Liu YJ, She Q. Diagnostic performance of noninvasive fractional flow reserve derived from coronary computed tomography angiography in coronary artery disease: a systematic review and meta-analysis. *Int J Cardiol* 184: 703–709, 2015.
- Fihn SD, Gardin JM, Abrams J, Berra K, Blankenship JC, Douglas PS, Foody JM, Gerber TC, Hinderliter AL, King SB, Kligfield PD, Krumholz HM, Kwong RYK, Lim MJ, Linderbaum JA, Mack MJ, Munger MA, Prager RL, Sabik JF, Shaw LJ, Sikkema JD, Smith CR, Smith SC, Spertus JA, Williams SV. 2012 ACCF/AHA/ACP/AATS/PCNA/SCAI/STS guideline for the diagnosis and management of patients with stable ischemic heart disease: a report of the American College of Cardiology Foundation/American Heart Association task force on practice guidelines, and the American College of Physicians, American Association for Thoracic Surgery, Preventive Cardiovascular Nurses Association, Society for Cardiovascular Angiography and Interventions, and Society of Thoracic Surgeons. *J Am Coll Cardiol* 60: e44–e164, 2012.
- Gonzalo N, Escaned J, Alfonso F, Nolte C, Rodriguez V, Jimenez-Quevedo P, Bañuelos C, Fernández-Ortiz A, García E, Hernandez-Antolin R, Macaya C. Morphometric assessment of coronary stenosis relevance with optical coherence tomography: a comparison with fractional flow reserve and intravascular ultrasound. *J Am Coll Cardiol* 59: 1080–1089, 2012.
- Grosskopf S, Biermann C, Deng K, Chen Y. Accurate, fast, and robust vessel contour segmentation of CTA using an adaptive self-learning edge model. *Proc SPIE* 7259: 72594D, 2009.
- Hachamovitch R, Di Carli MF. Methods and limitations of assessing new noninvasive tests. II. Outcomes-based validation and reliability assessment of noninvasive testing. *Circulation* 117: 2793–2801, 2008.
- Itu L, Sharma P, Mihalef V, Kamen A, Suciu C, Comaniciu D. A patient-specific reduced-order model for coronary circulation. In: *2012 9th IEEE International Symposium on Biomedical Imaging (ISBI)*. Barcelona, Spain: IEEE, 2012, p. 832–835.
- Itu L, Sharma P, Ralovich K, Mihalef V, Ionasec R, Everett A, Ringel R, Kamen A, Comaniciu D. Non-invasive hemodynamic assessment of aortic coarctation: validation with in vivo measurements. *Ann Biomed Eng* 41: 669–681, 2013.
- Itu L, Sharma P, Passerini T, Kamen A, Suciu C, Comaniciu D. A parameter estimation framework for patient-specific hemodynamic computations. *J Comput Phys* 281: 316–333, 2015.
- Kassab G, Fung YC. The pattern of coronary arteriolar bifurcations and the uniform shear hypothesis. *Ann Biomed Eng* 23: 13–20, 1995.
- Kassab GS. Scaling laws of vascular trees: of form and function. *Am J Physiol Heart Circ Physiol* 290: H894–H903, 2006.
- Kern MJ. Coronary physiology revisited practical insights from the cardiac catheterization laboratory. *Circulation* 101: 1344–1351, 2000.
- Koo BK, Erglis A, Doh JH, Daniels DV, Jegere S, Kim HS, Dunning A, DeFrance T, Lansky A, Leipsic J, Min JK. Diagnosis of ischemia-causing coronary stenoses by noninvasive fractional flow reserve computed from coronary computed tomographic angiograms: results from the prospective multicenter DISCOVER-FLOW (diagnosis of ischemia-causing stenoses obtained via noninvasive fractional flow reserve) study. *J Am Coll Cardiol* 58: 1989–1997, 2011.
- Koo BK, Yang HM, Doh JH, Choe H, Lee SY, Yoon CH, Cho YK, Nam CW, Hur SH, Lim HS, Yoon MH, Park KW, Na SH, Youn TJ, Chung WY, Ma S, Park SK, Kim HS, Tahk SJ. Optimal intravascular ultrasound criteria and their accuracy for defining the functional significance of intermediate coronary stenoses of different locations. *JACC Cardiovasc Interv* 4: 803–811, 2011.
- Kruk M, Wardziak L, Demkow M, Pleban W, Pregowski J, Dzielinska S, Witulski M, Witkowski A, Ruzyllo W, Kepka C. Workstation-based calculation of CTA-based FFR for intermediate stenosis. *JACC: Cardiovasc Imaging*. In press.
- Levin DC. Invasive evaluation (coronary arteriography) of the coronary artery disease patient: clinical, economic and social issues. *Circulation* 66: III71–III79, 1982.
- Mansi T, Georgescu B, Hussan J, Hunter PJ, Kamen A, Comaniciu D. Data-driven reduction of a cardiac myofilament model. In: *Functional Imaging and Modeling of the Heart*. New York: Springer, 2013, p. 232–240.
- Mantero S, Pietrabissa R, Fumero R. The coronary bed and its role in the cardiovascular system: a review and an introductory single-branch model. *J Biomed Eng* 14: 109–116, 1992.
- Meijboom WB, Van Mieghem CA, van Pelt N, Weustink A, Pugliese F, Mollet NR, Boersma E, Regar E, van Geuns RJ, de Jaegere PJ, Serruys PW, Krestin GP, de Feyter PJ. Comprehensive assessment of coronary artery stenoses: computed tomography coronary angiography versus conventional coronary angiography and correlation with fractional flow reserve in patients with stable angina. *J Am Coll Cardiol* 52: 636–643, 2008.
- Meuwissen M, Siebes M, Chamuleau SA, van Eck-Smit BL, Koch KT, de Winter RJ, Tijssen JG, Spaan JA, Piek JJ. Hyperemic stenosis resistance index for evaluation of functional coronary lesion severity. *Circulation* 106: 441–446, 2002.
- Min JK, Leipsic J, Pencina MJ, Berman DS, Koo BK, van Mieghem C, Erglis A, Lin FY, Dunning AM, Apruzzese P, Budoff MJ, Cole JH, Jaffer FA, Leon MB, Malpeso J, Mancini GB, Park SJ, Schwartz RS, Shaw LJ, Mauri L. Diagnostic accuracy of fractional flow reserve from anatomic CT angiography. *JAMA* 308: 1237–1245, 2012.

33. Morris PD, Ryan D, Morton AC, Lycett R, Lawford PV, Hose DR, Gunn JP. Virtual fractional flow reserve from coronary angiography: modeling the significance of coronary lesions: results from the VIRTU-1 (VIRTUal fractional flow reserve from coronary angiography) study. *JACC Cardiovasc Interv* 6: 149–157, 2013.
34. Murray CD. The physiological principle of minimum work. I. The vascular system and the cost of blood volume. *Proc Natl Acad Sci U S A* 12: 207–214, 1926.
35. Ng VG, Lansky AJ. Novel QCA methodologies and angiographic scores. *Int J Cardiovasc Imaging* 27: 157–165, 2011.
36. Nørgaard BL, Leipsic J, Gaur S, Seneviratne S, Ko BS, Ito H, Jensen JM, Mauri L, De Bruyne B, Bezerra H, Osawa K, Marwan M, Naber C, Erglis A, Park SJ, Christiansen EH, Kaltoft A, Lassen JF, Bøtker HE, Achenbach S. Diagnostic performance of noninvasive fractional flow reserve derived from coronary computed tomography angiography in suspected coronary artery disease: the NXT trial (analysis of coronary blood flow using CT angiography: next steps). *J Am Coll Cardiol* 63: 1145–1155, 2014.
37. Olufsen MS, Peskin CS, Kim WY, Pedersen EM, Nadim A, Larsen J. Numerical simulation and experimental validation of blood flow in arteries with structured-tree outflow conditions. *Ann Biomed Eng* 28: 1281–1299, 2000.
38. Papafaklis MI, Muramatsu T, Ishibashi Y, Lakkas LS, Nakatani S, Bourantas CV, Ligthart J, Onuma Y, Echavarria-Pinto M, Tsirka G, Kotsia A, Nikas DN, Mogabgab O, van Geuns RJ, Naka KK, Fotiadis DI, Brilakis ES, Garcia-Garcia HM, Escaned J, Zijlstra F, Michalis LK, Serruys PW. Fast virtual functional assessment of intermediate coronary lesions using routine angiographic data and blood flow simulation in humans: comparison with pressure wire-fractional flow reserve. *EuroIntervention* 10: 574–583, 2014.
39. Petraco R, Park JJ, Sen S, Nijjer SS, Malik IS, Echavarria-Pinto M, Asrress KN, Nam CW, Macias E, Foale RA, Sethi A, Mikhail GW, Kaprielian R, Baker CS, Lefroy D, Bellamy M, Al-Bustami M, Khan MA, Gonzalo N, Hughes AD, Francis DP, Mayet J, Di Mario C, Redwood S, Escaned J, Koo BK, Davies JE. Hybrid iFR-FFR decision-making strategy: implications for enhancing universal adoption of physiology-guided coronary revascularisation. *EuroIntervention* 8: 1157–1165, 2013.
40. Pijls NH. Fractional flow reserve after previous myocardial infarction. *Eur Heart J* 28: 2301–2302, 2007.
41. Pijls NH, de Bruyne B, Peels K, van der Voort PH, Bonnier HJ, Bartunek J, Koolen JJ. Measurement of fractional flow reserve to assess the functional severity of coronary-artery stenoses. *N Engl J Med* 334: 1703–1708, 1996.
42. Ralovich K, Itu L, Vitanovski D, Sharma P, Ionasec R, Mihalef V, Krawtschuk W, Zheng Y, Everett A, Pongiglione G, Leonardi B, Ringel R, Navab N, Heimann T, Comaniciu D. Noninvasive hemodynamic assessment, treatment outcome prediction and follow-up of aortic coarctation from MR imaging. *Med Phys* 42: 2143–2156, 2015.
43. Renker M, Schoepf UJ, Wang R, Meinel FG, Rier JD, Bayer RR, Möllmann H, Hamm CW, Steinberg DH, Baumann S. Comparison of diagnostic value of a novel noninvasive coronary computed tomography angiography method versus standard coronary angiography for assessing fractional flow reserve. *Am J Cardiol* 114: 1303–1308, 2014.
44. Ryan TJ. The coronary angiogram and its seminal contributions to cardiovascular medicine over five decades. *Circulation* 106: 752–756, 2002.
45. Samady H, Eshtehardi P, McDaniel MC, Suo J, Dhawan SS, Maynard C, Timmins LH, Quyyumi AA, Giddens DP. Coronary artery wall shear stress is associated with progression and transformation of atherosclerotic plaque and arterial remodeling in patients with coronary artery disease. *Circulation* 124: 779–788, 2011.
46. Sen S, Escaned J, Malik IS, Mikhail GW, Foale RA, Mila R, Tarkin J, Petraco R, Broyd C, Jabbour R, Sethi A, Baker CS, Bellamy M, Al-Bustami M, Hackett D, Khan M, Lefroy D, Parker KH, Hughes AD, Francis DP, Di Mario C, Mayet J, Davies JE. Development and validation of a new adenosine-independent index of stenosis severity from coronary wave-intensity analysis: results of the ADVISE (adenosine vasodilator independent stenosis evaluation) study. *J Am Coll Cardiol* 59: 1392–1402, 2012.
47. Sharma P, Itu L, Zheng X, Kamen A, Bernhardt D, Suciu C, Comaniciu D. A framework for personalization of coronary flow computations during rest and hyperemia. In: *2012 34th Annual International Conference of the IEEE Engineering in Medicine and Biology Society (EMBC)*. San Diego, CA: IEEE, 2012, p. 6665–6668.
48. Taylor CA, Fonte TA, Min JK. Computational fluid dynamics applied to cardiac computed tomography for noninvasive quantification of fractional flow reserve: scientific basis. *J Am Coll Cardiol* 61: 2233–2241, 2013.
49. Tøndel K, Indahl UG, Gjuvsland AB, Vik JO, Hunter P, Omholt SW, Martens H. Hierarchical cluster-based partial least squares regression (HC-PLSR) is an efficient tool for metamodeling of nonlinear dynamic models. *BMC Syst Biol* 5: 90–106, 2011.
50. Tonino PA, De Bruyne B, Pijls NH, Siebert U, Ikeno F, vant Veer M, Klauss V, Manoharan G, Engström T, Oldroyd KG, Ver Lee PN, MacCarthy PA, Fearon WF. Fractional flow reserve versus angiography for guiding percutaneous coronary intervention. *N Engl J Med* 360: 213–224, 2009.
51. Toth G, Hamilos M, Pyxaras S, Mangiacapra F, Nelis O, De Vroey F, Di Serafino L, Muller O, Van Mieghem C, Wyffels E, Heyndrickx GR, Bartunek J, Vanderheyden M, Barbato E, Wijns W, De Bruyne B. Evolving concepts of angiogram: fractional flow reserve discordances in 4000 coronary stenoses. *Eur Heart J* 35: 2831–2838, 2014.
52. Tröbs M, Achenbach S, Röther J, Redel T, Scheuering M, Winneberger D, Klöngenbeck K, Itu L, Passerini T, Kamen A, Sharma P, Comaniciu D, Schlundt C. Comparison of fractional flow reserve based on computational fluid dynamics modeling using coronary angiographic vessel morphology versus invasively measured fractional flow reserve. *Am J Cardiol* 117: 29–35, 2016.
53. Tu S, Barbato E, Köszegi Z, Yang J, Sun Z, Holm NR, Tar B, Li Y, Rusinaru D, Wijns W, Reiber JH. Fractional flow reserve calculation from 3-dimensional quantitative coronary angiography and TIMI frame count: a fast computer model to quantify the functional significance of moderately obstructed coronary arteries. *JACC Cardiovasc Interv* 7: 768–777, 2014.
54. Tu S, Bourantas CV, Nørgaard BL, Kassab GS, Koo BK, Reiber JH. Image-based assessment of fractional flow reserve. *EuroIntervention* 11: V50–V54, 2015.
55. van de Hoef TP, Nolte F, Damman P, Delewi R, Bax M, Chamuleau SA, Voskuil M, Siebes M, Tijssen JG, Spaan JA, Piek JJ, Meuwissen M. Diagnostic accuracy of combined intracoronary pressure and flow velocity information during baseline conditions adenosine-free assessment of functional coronary lesion severity. *Circ Cardiovasc Interv* 5: 508–514, 2012.
56. Wang R, Renker M, Schoepf UJ, Wichmann JL, Fuller SR, Rier JD, Bayer RR, Steinberg DH, De Cecco CN, Baumann S. Diagnostic value of quantitative stenosis predictors with coronary CT angiography compared to invasive fractional flow reserve. *Eur J Radiol* 84: 1509–1515, 2015.
57. Wilson RF, Wyche K, Christensen BV, Zimmer S, Laxson DD. Effects of adenosine on human coronary arterial circulation. *Circulation* 82: 1595–1606, 1990.
58. Windecker S, Kolh P, Alfonso F, Collet JP, Cremer J, Falk V, Filippatos G, Hamm C, Head SJ, Jüni P, Kappetein AP, Kastrati A, Knuuti J, Landmesser U, Laufer G, Neumann FJ, Richter DJ, Schauerte P, Uva MS, Stefanini GG, Taggart DP, Torracca L, Valgimigli M, Wijns W, Witkowski. 2014 ESC/EACTS Guidelines on myocardial revascularization. *Eur Heart J* 46: 517–592, 2014.
59. World Health Organization. *Global Status Report on Noncommunicable Disease 2010*. Geneva: World Health Organization, 2015.
60. Zamir M, Sinclair P, Wonnacott TH. Relation between diameter and flow in major branches of the arch of the aorta. *J Biomech* 25: 1303–1310, 1992.
61. Zheng Y, Barbu A, Georgescu B, Scheuering M, Comaniciu D. Four-chamber heart modeling and automatic segmentation for 3-D cardiac CT volumes using marginal space learning and steerable features. *IEEE Trans Med Imaging* 27: 1668–1681, 2008.
62. Zheng Y, Comaniciu D. *Marginal Space Learning for Medical Image Analysis*. New York: Springer, 2014.
63. Zhou Y, Kassab GS, Molloy S. On the design of the coronary arterial tree: a generalization of Murray's law. *Phys Med Biol* 44: 2929, 1999.